Impact performance of plate-like topological interlocking structures: Interlocking metrics for diverse designs

Siya Wang [a], Yi Min Xie [a,b] (iD), Y.X. Zhang [c], Xiaoshan Lin [a,*] (iD)

[a] Centre for Innovative Structures and Materials, School of Engineering, RMIT University, Melbourne, VIC 3000, Australia
[b] College of Future Technologies, Hohai University, Changzhou, Jiangsu 213200, China
[c] School of Mechanical and Mechatronic Engineering, University of Technology Sydney, NSW 2007, Australia

ARTICLE INFO

ABSTRACT

Topological interlocking (TI) structures emerge as a promising design strategy for advanced engineering applications, offering enhanced energy dissipation and localised failure modes. This study investigates the impact performance of plate-like TI structures composed of elements with curved interfaces, focusing on the effects of two distinct geometric design factors: base polygon shape and interface morphology. Four interlocking metrics, including contact area, contact area ratio, Gaussian curvature, and critical inclination angle factor, are proposed to quantitatively assess the mechanical performance of these structures. Finite element simulations are employed to evaluate their behaviour under various drop heights, analysing energy dissipation, stress distribution, and deformation characteristics. Simulation results reveal that the base polygon shape significantly influences contact area and load transfer efficiency, while interface morphology affects stress dispersion and deformation behaviour. Strong correlations are found between the proposed geometric metrics, including contact area, contact area ratio, and critical inclination angle factor, and key mechanical responses like energy dissipation and maximum displacement. In particular, larger critical inclination angle factors promote broader stress propagation and improve energy absorption. Additionally, regions with high Gaussian curvature align with stress concentrations and failure initiation, providing a basis for predicting failure zones and guiding reinforcement design. These findings provide a quantitative foundation for optimising TI structures under impact loading.

1. Introduction

The standard approach in engineering design typically relies on monolithic structural elements. However, there is growing recognition of the benefits of segmented or fragmented designs, particularly for enhancing structural adaptability and resilience [1]. A prospective solution in this area is the concept of topological interlocking (TI), a method that has evolved over the past decades. TI refers to the arrangement of specially shaped elements, which achieve global stability through peripheral constraints and local stability through their geometric interplay and positioning, thereby establishing kinematic constraints [2]. TI structures offer a range of advantages such as enhanced flexibility, localised failure patterns, greater energy absorption, and ease of assembly [3–8], rendering them highly adaptable for a variety of civil engineering applications [9–14]. Notably, TI structures have also demonstrated impact resistance up to ten times greater than that of monolithic structures [15], making them highly advantageous in

applications requiring high energy dissipation and structural integrity, such as protective shieldings [16], crash-resistant panels [17], and aerospace components [4]. Therefore, understanding and optimising the impact performance of TI structures is critical for their effective deployment in dynamic and extreme loading environments.

The TI element designs can be classified into three categories based on their geometric characteristics: polyhedral elements, elements with curved interfaces, and bio-inspired elements [18]. Among these, TI elements with curved interfaces stand out as a promising alternative for improving structural stability and energy dissipation capacity [19,20]. Also, the curved contact surfaces of these elements enable greater flexibility in deflection and support multi-layer configurations while reducing reliance on material friction [21]. The osteomorphic element, proposed by Dyskin et al. [1] and featuring two concavo-convex curved side surfaces, is the first TI element with curved interfaces. This element enables the construction of a cohesive multi-layer structure by aligning its protrusions and recesses. The interlocking mechanism is achieved

---

* Corresponding author.
  E-mail address: susanna.lin@rmit.edu.au (X. Lin).

through the mutual jamming of these features under confining loads. This foundational work established the basis for further exploration into the potential of curved interface designs. Through indentation tests and numerical analyses, Dyskin et al. [6,19,22] demonstrated that structures assembled from these elements exhibited superior structural integrity and resistance to failure. Unlike polyhedral assemblies, which deform through the pullout of central elements, the assemblies with curved interfaces possessed a more flexible and ductile deformation mode.

Later, research efforts have expanded on the concept of TI elements with curved interfaces. Djumas et al. [23] explored the use of hierarchical interfaces in TI assemblies and demonstrated, through point loading tests, that this approach enhanced load-bearing capacity. Also, structural performance could be optimised by tailoring geometrical features and adjusting the interaction mechanism between elements. Rezaee Javan et al. [24] introduced an interlocking brick with four concavo-convex side surfaces and conducted drop weight tests to analyse the impact response of the interlocking assembly plates. The study revealed that the design significantly improved flexural performance and energy absorption, and effectively prevented catastrophic failure by constraining crack propagation. Xu et al. [16] proposed a novel tunnel lining design composed of concrete TI elements characterised by six concave-convex interfaces. Employing lab-scale drop weight tests, they demonstrated the design's efficacy in resisting joint opening and maintaining structural integrity. Later, they evaluated the influence of geometry on dynamic performance and provided design recommendations for enhanced structural resilience [25]. The potential of hierarchical design in beam-like topological interlocking structures with sinusoidal surfaces was explored by Koureas et al. [26]. Numerical simulations demonstrated that optimised surface curvature and gradient enhanced effective friction, allowing structures to achieve theoretical strength and toughness with realistic friction coefficients.

The mechanical performance and failure modes of TI structures are significantly influenced by geometric parameters. To quantify this, Dalaq and Barthlet [27] proposed a waviness parameter that described polynomial interface curvature, showing a linear relationship between mechanical performance (including overall strength and toughness) and element interface curvature. Koureas et al. [26] suggested a combined surface measure, defined as the product of surface curvature and gradient, to quantify the interlocking efficacy of hierarchically interfaced beam-like TI structures. Furthermore, for planar structures composed of hierarchically interfaced elements, the inclination angle of the first protrusion from the top surface exhibited a linear relationship with toughness and strength, as demonstrated in a study reported in [28]. Additionally, an interlocking effect parameter, based on the ratio of amplitude to element edge length for osteomorphic elements, was proposed by Schapira et al. [9]. This parameter reflected contact surface convexity and aided in evaluating the blast resistance of TI column structures. The aforementioned parameters effectively quantify the mechanical performance of TI structures by linking strength and toughness to geometric features. However, their derivation, based on specific geometries and assumptions, limits their generalisability and applicability to a wider range of interface designs. This highlights the need for the development of more versatile and computationally efficient measures.

Although prior studies have investigated TI structures with curved interfaces, research has primarily focused on specific geometries or isolated metrics for assessing interlocking effects. The existing metrics are often limited by their dependence on particular interface designs, hindering broader applicability. Furthermore, while TI structures have been found to have enhanced flexibility, energy absorption, and structural integrity, most previous investigations have concentrated on quasi-static behaviour, leaving their dynamic response inadequately explored. To address these gaps, this study investigates the influence of geometric characteristics of individual TI elements on the dynamic response of assembled structures under impact loading. 12 designs of TI elements are developed based on different polygon shapes and interface

morphologies. Four metrics, including Gaussian curvature, contact area, contact area ratio, and critical inclination angle factor, are proposed to quantitatively assess interlocking efficacy. These metrics establish a correlation between the geometric attributes of individual elements and the impact performance of the assembled structures, emphasising energy dissipation, deformation modes, stress distribution, and failure patterns. Key findings reveal that polygons with fewer edges facilitate balanced stress transfer, whereas a higher number of edges can lead to localised failures. Energy dissipation and displacement show strong correlations with the contact area (and its ratio of flat surface area) and the critical inclination angle factor, while effective stress distribution over the interfaces is closely linked to the Gaussian curvature. These correlations validate the proposed metrics as comprehensive measures for assessing and optimising interlocking performance.

The methodology of this study is detailed in Section 2, providing an overview of the design approach for TI elements and the derivation of metrics to quantify interlocking effectiveness. Section 3 introduces the numerical simulation method employed to study the impact behaviour of TI plates, with validation against previous experimental data. Section 4 focuses on assessing the impact performance of TI structures and examining the effectiveness of the proposed interlocking metrics. Finally, Section 5 summarises the research findings and offers design recommendations derived from the outcomes.

2. Design strategies for TI elements and key parameters

2.1. Design of TI elements

In the authors' previous study [29], a generalised design framework for TI elements with curved interfaces has been proposed, which includes three principal steps: 1) the selection of a simple-to-construct monomorphic polygonal prototile, 2) the application of a curve function $f(x)$ to shape polygon edges into concavo-convex profiles [Fig. 1 (a)], and 3) the lofting of the curved edges to generate interfaces conducive to effective interlocking [Fig. 1(b)]. The design parameters include the polygonal shape, edge length, curve function, and element height, as shown in Fig. 1(c). This approach enables the development of TI elements from various polygonal tilings and interface generation techniques. In this study, this approach is employed. A sinusoidal function, as given in Eq. (1), is used as the controlling function for the curvature of the edges.

$$f(x) = A\sin(k\frac{\pi x}{a}), k \epsilon Z \tag{1}$$

where x is the position along the edge; a refers to the edge length; A is the amplitude, representing the peak deviation of the curve from the edge; k is the wave number, which controls the number of protrusions and recesses, and k must be an integer.

To investigate the influences of polygon shape and interface morphology on the impact performance of TI structures, 12 TI element designs are created and divided into two groups in this study. The first group of elements are designed from six different base polygonal tilings [Fig. 2(a)], i.e., regular triangle, square, regular hexagon, parallelogram (aspect ratio: $\sqrt{2}:1$), Barn pentagon (planigon), and rectangle (aspect ratio: $2:1$). The TI element created based on square tiling serves as a benchmark for comparison. This reference element is characterised by an edge length of $a = 50$ mm, a height of $h = a/2 = 25$ mm, and a curve function defined by $f(x) = 6\sin 2\frac{\pi x}{a}(x \in [0, a])$. The amplitudes of the curve functions for the other designs are adjusted to maintain uniformity in height, volume, and interface morphology, as shown in Fig. 2(b).

To explore the influence of variations in interface morphology and additional edge controls, the second group consists of six TI elements: three are derived using different curve functions, and the other three are created with supplementary interface techniques, as shown in Fig. 3. A square tiling with an edge length of $a = 50$ mm and a height of $h = 25$
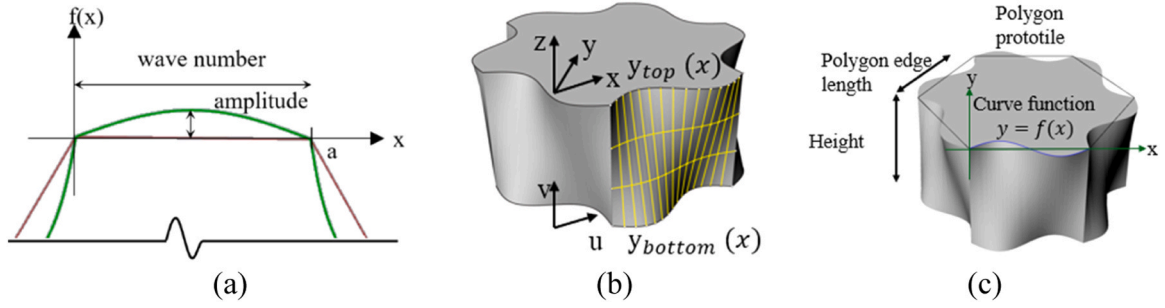
Fig. 1. Schematic illustration of the general design method for creating new TI elements [29]: (a) curve function, (b) interface generated by lofting, and (c) design parameters.
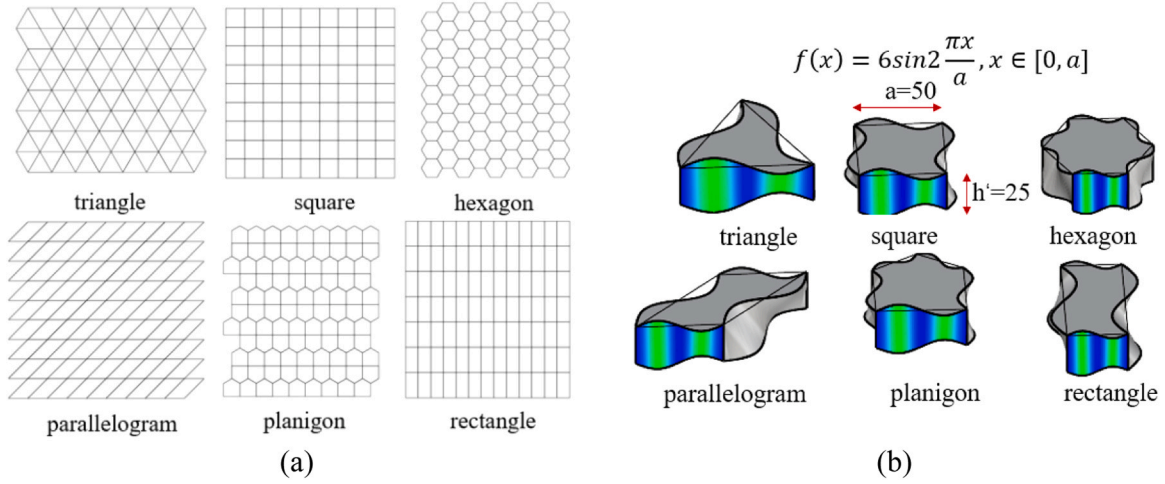

Fig. 2. TI elements created based on different polygon shapes: (a) polygon tilings, and (b) element geometries and their Gaussian curvatures.
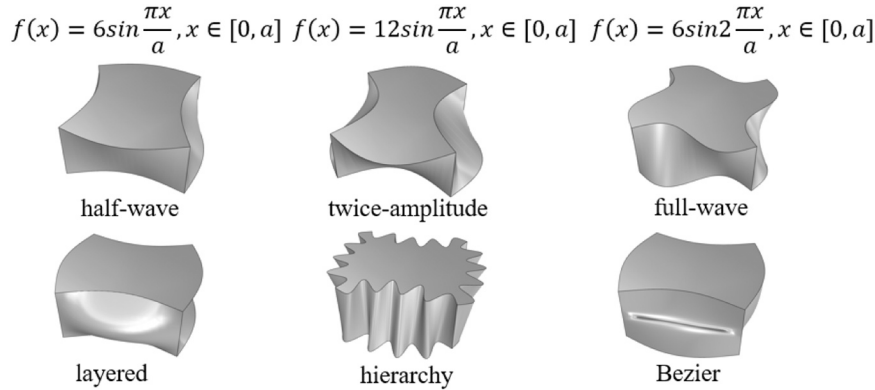

Fig. 3. TI elements with different interface morphologies.

mm is used for all designs within this group. Fig. 4 shows details of the supplementary interface techniques. The layered technique, as shown in Fig. 4(a), involves configuring the element using top, medial, and bottom control edges. Notably, a medial control edge with pronounced convexity relative to the top and bottom edges is incorporated, creating a multi-level curvature that enhances the concavo-convex interlocking mechanism. Fig. 4(b) shows the hierarchy method, which modifies the element edges using a compound sinusoidal function. In this process, the original black straight edge is transformed into the green curved shape through two successive modifications, each applying a distinct sinusoidal function. In Fig. 4(c), a symmetrical Bezier curve is introduced in the middle of the element interface. The curvature of this curve is governed

by the edge curve function and the angle α formed between the intermediate control points of the Bezier curve.

2.2. Metrics for assessing interlocking effect

In this paper, four metrics are proposed to quantitatively assess the interlocking effect, which are contact area, contact area ratio, Gaussian curvature, and critical inclination angle factor. These metrics are formulated to distinguish between polygon shapes and to appraise the effect of interface morphology.
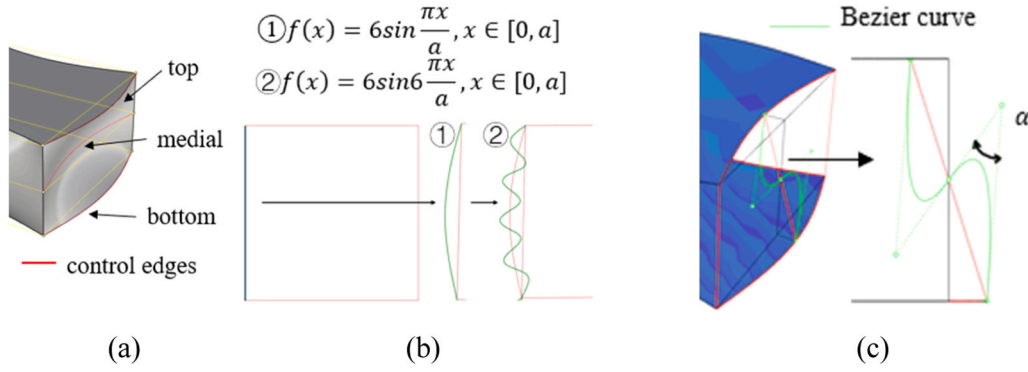
Fig. 4. Three supplementary interface techniques: (a) layered technique with medial control curve, (b) hierarchy modification on edges, and (c) Bezier curve.

2.2.1. Contact area and contact area ratio

The contact area A_c refers to the total area of the curved interfaces of a single element, and the contact area ratio A_c/A_f is a dimensionless measure indicating the ratio of the contact area to the flat surface area, where the flat surface area A_f is defined as the combined area of the element's top and bottom flat surfaces. The curved interfaces and flat surfaces are shown in Fig. 5. Given the consistency of element volume, height, and interface morphology within the first group, variations in the contact area are attributed solely to the polygon shape. This renders the contact area an effective metric for capturing shape-specific features. The methodology for calculating both the contact area and the contact area ratio is detailed in the Appendix.

Table 1 summarises the calculated contact area and contact area ratio results for the first group of TI elements. The element with a triangular base polygon exhibits the largest contact area and highest contact area ratio, indicating the most extensive interlocking contact relative to its footprint. In contrast, the element derived from a hexagonal base polygon has the smallest contact area and lowest contact area ratio, suggesting the least interlocking contact. These findings highlight the critical influence of the base polygon shape on contact efficiency, with shapes having fewer edges generally achieving higher ratios, leading to more effective surface interactions.

2.2.2. Gaussian curvature

In the studies on lattice structures and biological tissues [30–32], Gaussian curvature has been used as an effective parameter to assess the influence of surface curvature on structural mechanical performance. Inspired by these studies, Gaussian curvature K is employed in this research to quantify contact surface interlocking behaviour. Defined as the product of the two principal curvatures ($K = k_1 k_2$), Gaussian curvature provides a mathematical basis for classifying surface points as concave ($K > 0$), planar ($K = 0$), or convex ($K < 0$). This method can effectively capture the three-dimensional characteristics of surface morphology, surpassing the limitations of two-dimensional parameters, such as waviness and inclination measurements, used in previous studies [26–28]. The Gaussian curvature distribution over the contact surfaces of TI elements in the second group is obtained using "Curvature

Fig. 5. Illustration of contact area ratio.

Analysis" in Rhino and examined as an effective indicator of stress distribution across interfaces. A detailed analysis is presented in Section 4.2.2.

2.2.3. Critical inclination angle factor

In this work, a metric called the critical inclination angle factor is proposed, which is designed to evaluate the slope at the midpoint of the edge on the compressive side of the interface, as indicated by the red point in Fig. 6. Specifically designed for TI structures with curved interfaces, this factor quantifies interlocking performance by capturing their deformation characteristics under out-of-plane loading. Unlike previous studies that often utilised wavy surface inclination [28], the proposed critical inclination angle factor focuses on the compressive side, where plate-like bending causes compression and collision between adjacent elements, while tension and separation occur on the opposite side.

The critical inclination angle factor $\tan^2\theta_c$ is defined as the sum of the squares of the horizontal ($\tan\theta_h$) and vertical ($\tan\theta_v$) inclination components, expressed as: $\tan^2\theta_c = \tan^2\theta_h + \tan^2\theta_v$. This metric is rationalised based on the interplay between deformation energy and element geometry, as derived from a theoretical model. The overall energy dissipation capacity of a structure is mainly governed by the strain energy within individual elements during deformation induced by contact. This energy is strongly influenced by the element geometry, as it determines both the contact region and the degree of interlocking between adjacent elements during relative sliding. According to [33], the relationship between strain energy and element geometry can be expressed:

$$U = \frac{1}{2}EV\varepsilon^2 = \frac{1}{2}E\int_{z=0}^{h-\delta}\varepsilon_{xx}^2 A_z \mathrm{d}z \qquad (2)$$

where U represents the elastic strain energy within the material, E is the elastic modulus, V is the volume of the element, ε means the average strain, δ is the displacement, ε_{xx} is the nominal strain in the x direction, and A_z is the cross-sectional area of the element at height z.

Different from the polyhedral element studied in [33], which has inclination in a single direction, the TI element with curved interfaces in this study features inclinations in both in-plane and out-of-plan directions. The in-plane inclination primarily affects lateral sliding resistance, while the out-of-plane inclination influences vertical compression and separation under loading. Thus, the total energy is determined by incorporating the contributions from both directions, as given by Eq. (3). This decoupled energy formulation is grounded in well-established engineering standards and theoretical frameworks that treat directional effects independently. For example, seismic design codes such as GB 50011–2010 [34] and ASCE 7–22 [35] assume statistical independence between seismic actions. Similarly, structural mechanics principles, including the von Mises criterion and bi-axial bending stress combination methods in Eurocode EN 1993–1–1 [36,37], simplify multi-axial
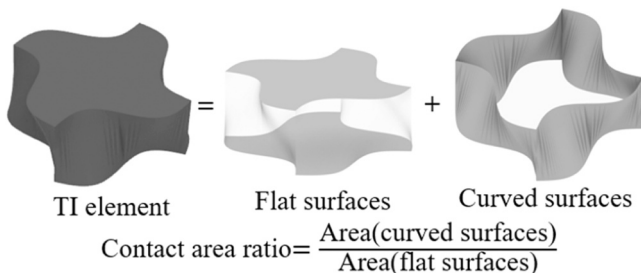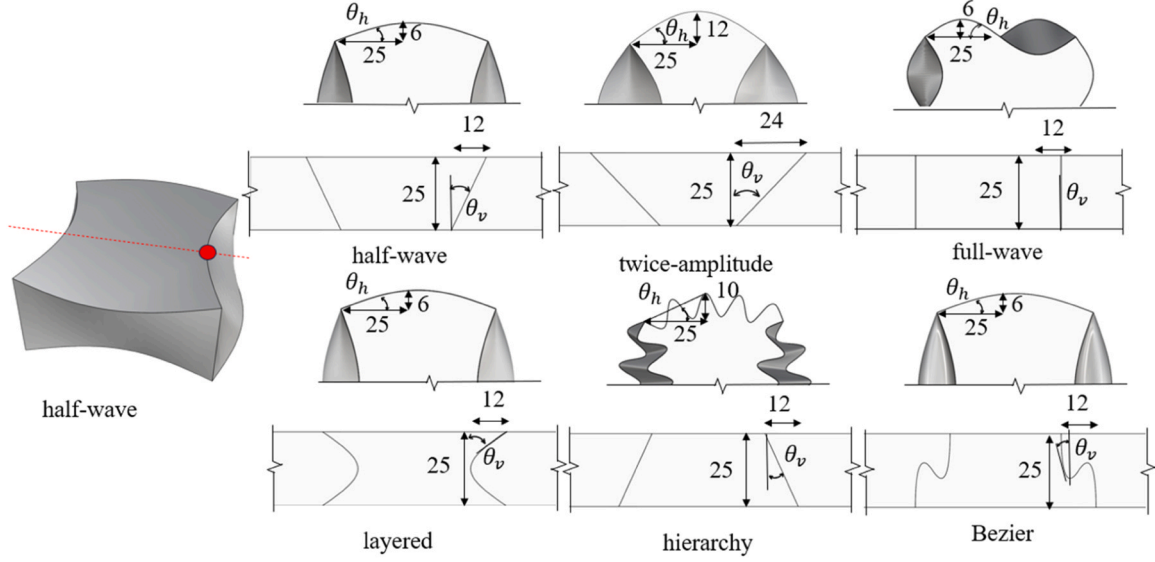
Table 1
Summary of contact area and contact area ratio of the first group elements.

	Triangle	Parallelogram	Rectangle	Planigon	Square	Hexagon
Contact area A_c (mm^2)	6584	6036	5197	4830	5000	4700
Contact area ratio A_c/A_f	1.32	1.2	1.08	0.97	1	0.92

Fig. 6. Position of critical inclination angle and its in-plane and out-of-plane components in TI elements.

stress states through scalar superposition. Furthermore, in structural dynamics, energy contributions from individual modes are evaluated independently and superimposed to obtain the overall system response [38].

$$U = U_{xx}^z + U_{xx}^y \tag{3}$$

where U_{xx}^z and U_{xx}^y represent the strain energy associated with the normal strain ε_{xx}, induced by inclinations in the z direction and y direction, respectively.

This can be further expressed in terms of the strain components ε_{xx}^y and ε_{xx}^z as follows:

$$U = \frac{1}{2}E \int_{z=0}^{z=h-\delta} (\varepsilon_{xx}^y)^2 A_z dz + \frac{1}{2}E \int_{z=0}^{z=h-\delta} (\varepsilon_{xx}^z)^2 A_z dz \tag{4}$$
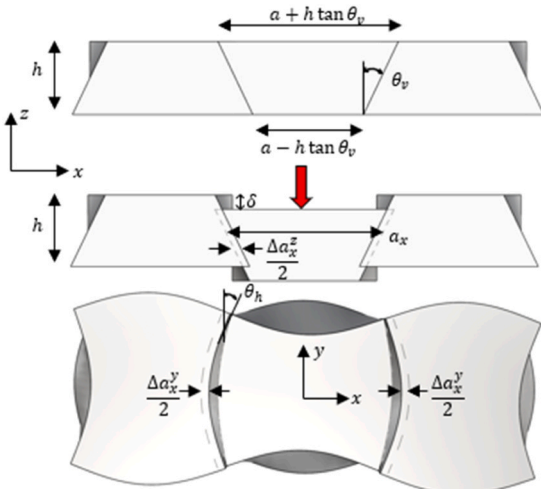
Fig. 7. Kinematic model for element deformation.

As shown in Fig. 7, the strains ε_{xx}^z and ε_{xx}^y can be expressed as a function of the inclination angles:

$$\varepsilon_{xx}^z = \frac{\Delta a_x^z}{a_x} = \frac{-2\delta\tan\theta_v}{a - (h - 2\delta - 2z)\tan\theta_v} \tag{5a}$$

$$\varepsilon_{xx}^y = \frac{\Delta a_x^y}{a_x} = \frac{-2\delta\tan\theta_h}{a - (h - 2\delta - 2z)\tan\theta_h} \tag{5b}$$

where $\Delta a_x^i = -2\delta\tan\theta_j$ ($i = z$ or $y; j = v$ or h) represents projected dimensional change in the x-direction due to inclination in either the z-direction or the y-direction under the displacement δ, and $a_x = a - (h - 2\delta - 2z)\tan\theta_j$ is the projected element length in the x-direction at height z.

Define

$$t = a - (h - 2\delta - 2z)\tan\theta_j \tag{6}$$

Taking the derivative

$$dt = 2\tan\theta_j dz \tag{7}$$

Thus, the integral in Eq. (4) can be expressed as

$$I = \int_{t=a-(h-2\delta)\tan\theta_j}^{t=a+h\tan\theta_j} \frac{4\delta^2\tan^2\theta_j}{t^2} \frac{A_z}{2\tan\theta_j} dt = 2\delta^2\tan\theta_j A_z \int_{t=a-(h-2\delta)\tan\theta_j}^{t=a+h\tan\theta_j} \frac{dt}{t^2}$$

$$= 2\delta^2\tan\theta_j A_z \left[-\frac{1}{a + h\tan\theta_j} + \frac{1}{a - (h - 2\delta)\tan\theta_j} \right] \tag{8}$$

Therefore,

$$U = \sum E\delta^2\tan\theta_j A_z \left[\frac{1}{a - (h - 2\delta)\tan\theta_j} - \frac{1}{a + h\tan\theta_j} \right] \tag{9}$$

Fig. 8 shows the relationship between the energy and the critical inclination angle factor $\tan^2\theta_c$, $h = 25$ mm, $a = 50$ mm, $z \in [0, h]$, $\tan\theta_h \in [0, 1)$, $\tan\theta_v \in [0, 2)$, and δ ranging from 0.1 mm to 10 mm.
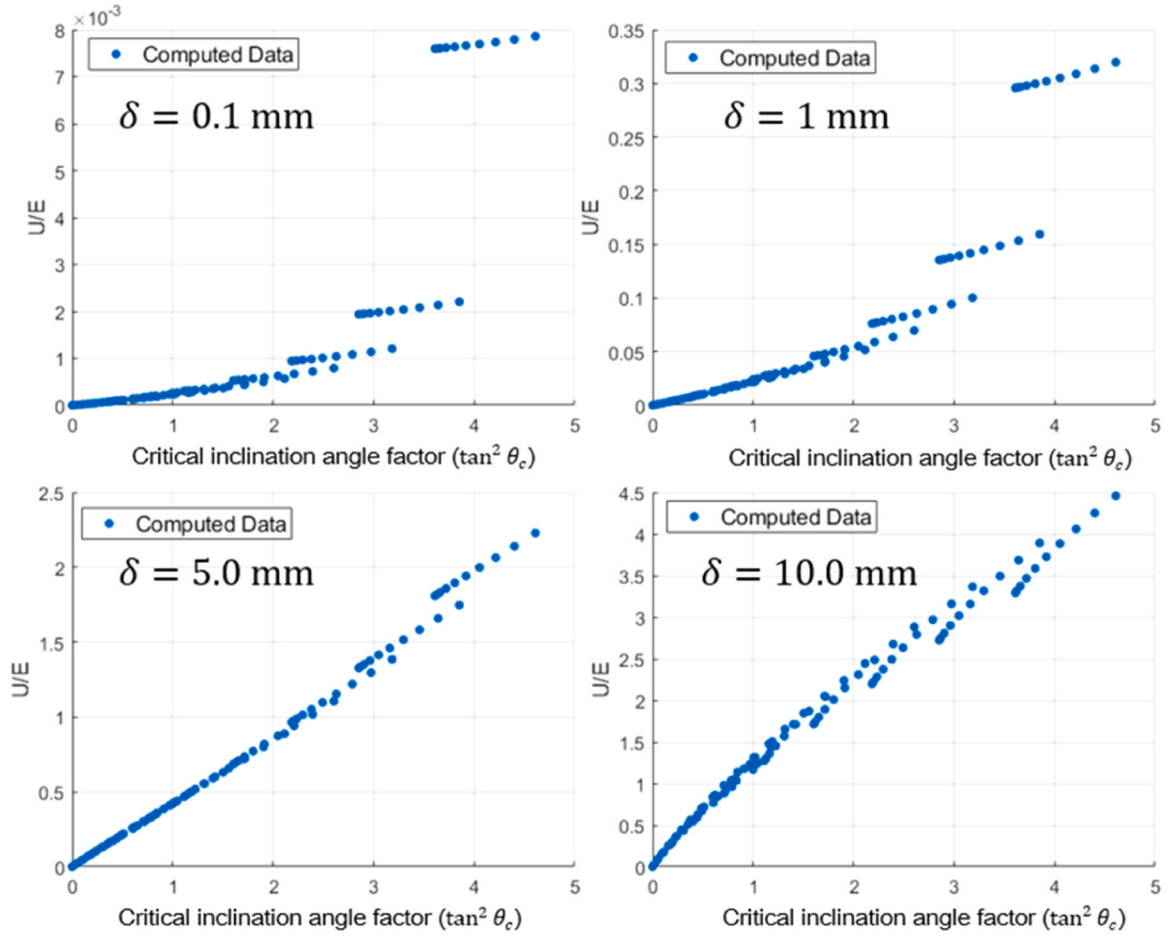
Fig. 8. Relationship between total energy and critical inclination angle factor.

The ranges of $\tan\theta_v$ and $\tan\theta_h$ are governed by the element geometry, while the central displacement δ is determined based on deformation limits observed in finite element simulations and experiments, capturing the operational deformation range of the structure. It can be seen that the total energy increases with the critical inclination angle factor, and this relationship is nearly linear when $\tan\theta_j$ is small. As a result, the critical inclination angle factor $\tan^2\theta_c$ correlates with energy dissipation, with higher values generally leading to greater energy dissipation. This suggests enhanced interlocking and resistance to failure, making the critical inclination factor a useful metric for evaluating interlocking performance. Table 2 summarises the calculated critical inclination angle factors for the TI elements in the second group.

3. Finite element model and validation

In this study, LS-DYNA is used to establish finite element (FE) model for investigating the structural performance of TI assemblies under impact loading, as demonstrated in Fig. 9. The simulation involves a 400 mm × 400 mm × 25 mm plate-like assembly of concrete TI elements with a compressive strength of 28.6 MPa, subjected to impacts
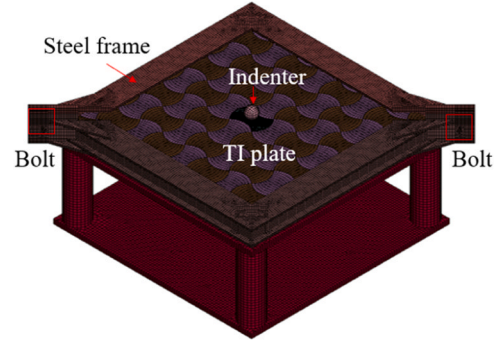

Fig. 9. FE model for TI assembly under impact.

from a spherical indenter dropped from heights ranging from 0.4 to 2.0 m. To replicate the boundary conditions in the experiments [39], different confining torques (5 Nm and 10 Nm) are applied to the supporting steel frame during the model validation phase. These variations allow for assessing the model's capability in capturing the load transfer behaviour, deformation patterns, and failure modes observed in physical tests. A comprehensive investigation into the influence of confining torque has been reported in previous research [39]. In the present model, the nodes at the two bolt locations on the supporting frame are restrained in both vertical and horizontal directions. The initial axial forces of 2.5 kN and 5 kN, corresponding to equivalent torque levels of 5 Nm and 10 Nm, respectively, are applied using the "INITIAL_AX-IAL_FORCE_BEAM". The steel frame is simulated using an elastic

Table 2
Critical inclination angle factors of the TI elements in the second group.

	Half-wave	Twice-amplitude	Full-wave	Layered	Hierarchy	Bezier
Critical inclination angle factor $\tan^2\theta_c$	0.56	1.12	0.25	1.03	0.64	0.56

material model (MAT 001), consistent with its experimentally informed, sufficiently large design, which ensures that stresses remain well below yield strength and its deformation is negligible compared to that of the concrete elements. The 25-mm-diameter spherical indenter is modelled using a rigid material model (MAT20). The continuous surface cap model (CSCM) is employed to capture the behaviour of concrete under dynamic loading. The CSCM incorporates key nonlinear mechanisms, including damage-based softening, modulus reduction, shear dilation and compaction, strain-rate effect, and the influence of confinement, providing a comprehensive constitutive representation for modelling concrete elements. The model requires only three primary inputs (compressive strength, maximum aggregate size, and unit system), with remaining parameters internally calibrated based on an extensive material database [40,41]. The strain rate sensitivity is accounted for by activating the rate-dependent formulation with rate parameter set to 1, ensuring that the dynamic strength enhancement of concrete is accurately captured through the model's built-in rate-dependent viscoplastic overstress formulation [42]. Previous studies [39,43] have validated CSCM's predictive capability in dynamic impact scenarios. The failure of concrete elements is represented using an erosion coefficient ($ERODE =$ 1.10), which is triggered when the maximum principal strain surpasses 0.10, consistent with recommended practices [41]. Table 3 summarises the key parameters for the material models. In the present model, the contact interactions are defined using the "Automatic_Surface_To_Surface" algorithm in LS-DYNA. A friction coefficient of 0.4 is assigned to the interfaces between TI element, while the contacts between the indenter and the TI elements, as well as between the steel frame and the TI elements, are assumed to be frictionless. This approach aligns with established modelling practices in previous studies [39,44]. In the present model, a finer mesh (0.75 mm) is applied to the central TI element, which measures approximately 50 mm × 50 mm, located directly beneath the indenter to accurately capture the failure of concrete, while a coarser mesh (2.5 mm) is applied in other areas to improve computational efficiency. Concrete is modelled using solid elements, with hourglass control implemented via the Flanagan–Belytschko stiffness-based approach. Please note that the deformation plots in Fig. 14 are scaled by a factor of 10 for clarity. The energy dissipation is determined by the change in the kinematic energy of the indenter before and after impact, which reflects the total energy absorbed by the TI assembly through deformation and interfacial mechanisms. The model is validated against the experimental results reported in [24].

The experimental test conditions and the FE model settings are summarised in Table 4. The calculated mechanical performance and damage distributions are shown in Fig. 10. It can be seen from Fig. 10(a) that both impact force and indenter displacement histories obtained from the FE model closely align with the experimental data across all loading scenarios. Furthermore, the typical damage patterns and crack distributions calculated by the FE model are in good agreement with experimental observations. The effective plastic strain contours accurately capture the primary damage locations and crack patterns in the central brick, as observed in TIP-2 [Fig. 10(b)].

4. Evaluation of interlocking metrics

In this section, the interlocking metrics discussed in Section 2.2 are

Table 4
Summary of experimental [39] and numerical configurations.

Specimen	Torque (Nm)	Nominal height of mass (mm)	Equivalent initial axial force in connecting bolts in FEM (N)	Equivalent initial velocity of indenter in FEM (m/s)	Incident energy (J)
TIP[a]−1	5	400	2500	2.9	13.5
TIP−2	10	1200	5000	4.8	37.6
TIP−3	10	2000	5000	6.1	60.9

[a] TIP: Topological interlocking plate.

evaluated through a comparative analysis of the impact responses of TI structures assembled with the two groups of TI elements, using the FE model validated in Section 3. These TI assemblies are subjected to impacts from an indenter dropped from heights of 1.0 or 3.0 m under a constant confining load generated by 10 Nm torque. The response of a monolithic plate with identical dimensions and concrete material is also simulated for comparison.

4.1. TI elements with different base polygon shapes

4.1.1. Mechanical performance and interlocking metrics

This section examines the mechanical responses of TI structures with different base polygon shapes (the first group) under impact loading. The analysis examines energy dissipation, maximum indenter displacement, impact force-displacement behaviour of the plate, and stress distribution, aiming to elucidate the influences of geometric features and interlocking metrics on structural performance. A 1 m drop height is selected to simulate moderate impact scenarios commonly found in structural applications, such as protective barriers, crash structures, and impact-resistant panels [45]. Fig. 11 presents the relationship between energy dissipation and maximum indenter displacement, as well as the impact force-displacement response of TI plates with different base polygon shapes. As shown in Fig. 11(a), the energy dissipation ranking for TI structures with different base polygon shapes, from highest to lowest, is as follows: triangle > parallelogram > rectangle > planigon > square > hexagon. The maximum indenter displacements align with this order. The triangular element-based structure demonstrates the greatest deformation capacity, consequently, resulting in the highest energy dissipation.

By comparing the impact force-displacement curves in Fig. 11(b), it is evident that all TI plates exhibit lower impact forces and undergo larger displacements than the monolithic plate. The monolithic response begins with a steep, near-linear rise in force with increasing displacement, followed by softening as cracking develops. Upon rebound, displacement decreases and a second force peak emerges during unloading before contact is lost and the force collapses toward zero. In contrast, the TI plates exhibit a more compliant response. As the number of edges in the base polygon increases, the mechanical behaviour of the TI plates gradually shifts toward that of the monolithic structure. This phenomenon can be attributed to the increase in constrained boundaries as the base polygon's edge count rises. A greater number of constrained edges enhances the stiffness of individual elements, resulting in overall

Table 3
Summary of key parameters of the material models.

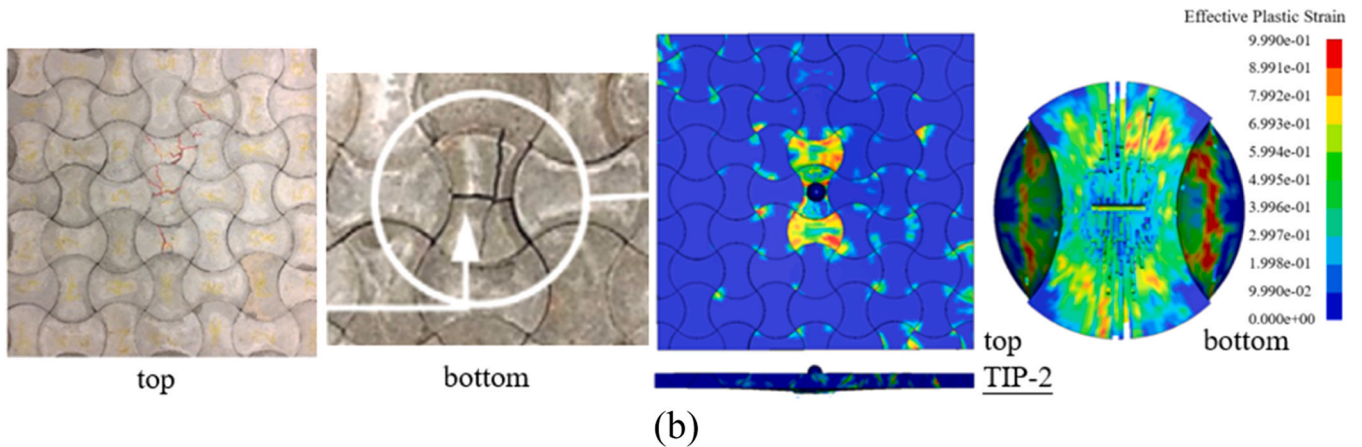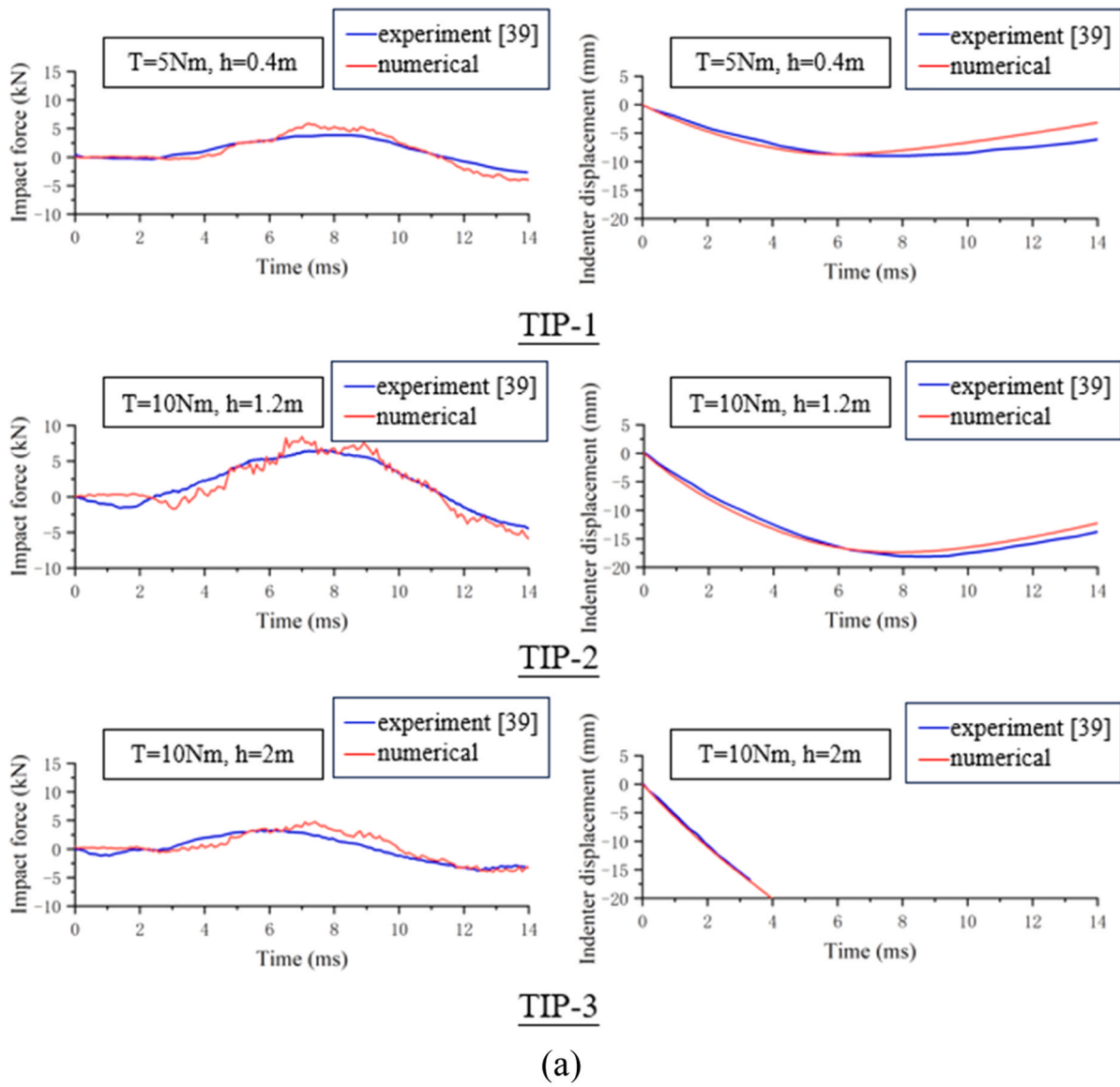| Material model		Key parameters				
CSCM (MAT159)	Density (g/mm^3)	Compression strength (MPa)	NPLOT	Rate effect	Erode	Maximum aggregate size (mm)
	2.1E-3	28.6	1	1	1.10	2.0
Elastic (MAT001)	Density (g/mm^3)	Elastic modulus (GPa)			Poisson ratio	
	7.83E−3	2E5			0.3	
Rigid (MAT20)	Density (g/mm^3)	Elastic modulus (GPa)			Poisson ratio	
	4.15E−1	2E5			0.3	

Fig. 10. Comparison of numerical simulation results and experimental data: (a) impact force-time curves and indenter displacement-time curves, and (b) comparison of damage distributions in TIP-2 between experimental result [24] and numerical simulation.

mechanical performance becoming closer to that of a monolithic plate.

Fig. 12 shows the stress distributions on the bottom surfaces of the TI assemblies in the first group. The plate with triangular base polygon shape demonstrates the most uniform stress distribution, as evidenced

by larger areas experiencing stress with smaller variation. This uniformity indicates improved load transfer efficiency, which reduces localised stress concentrations within certain elements (e.g., the central elements in the TI plate with a hexagonal base polygon shape) that could
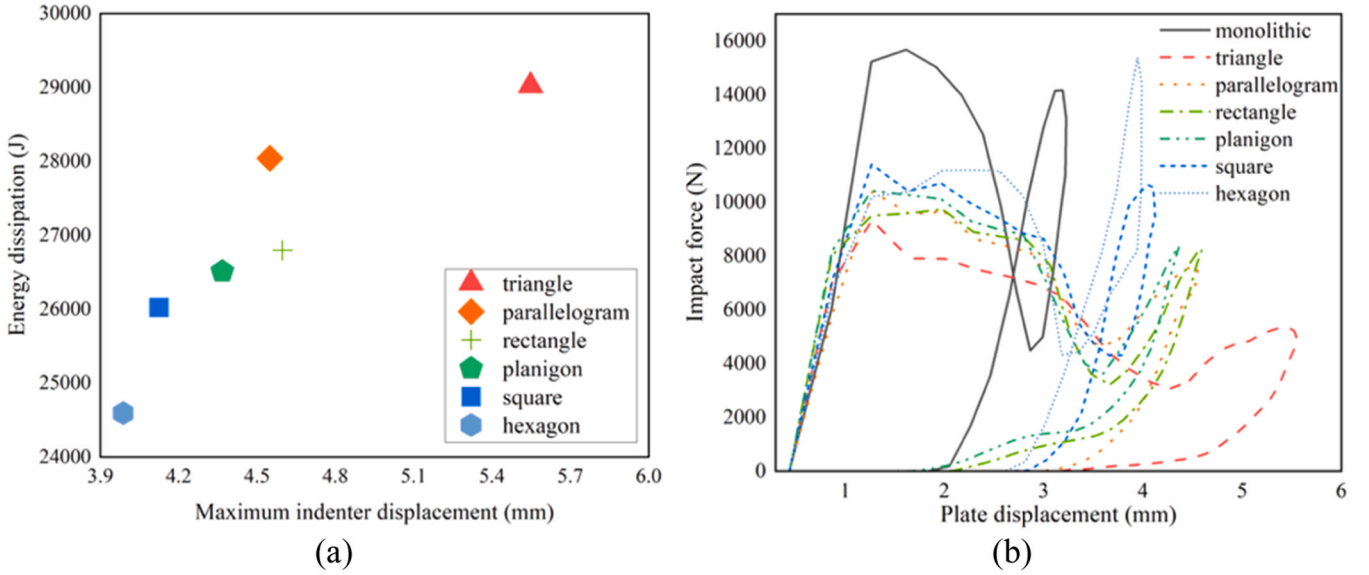
(a)   (b)

Fig. 11. Energy dissipation-maximum indenter displacement relationships and impact force-displacement curves of the first group of TI structures at a drop height of 1.0 m.
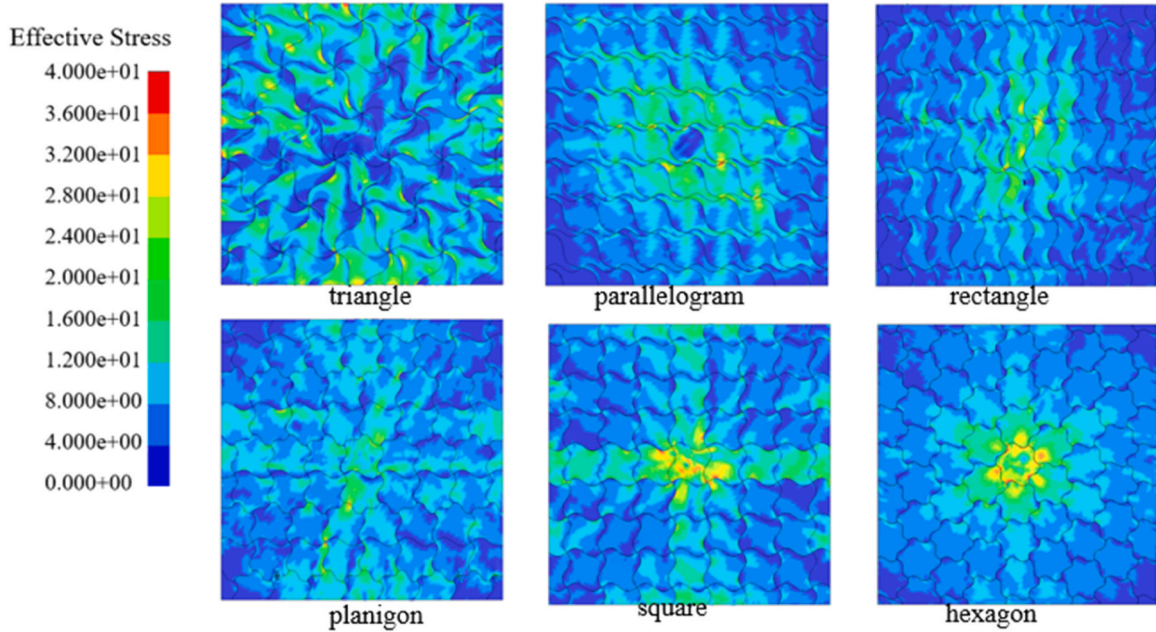

Fig. 12. Stress distributions on the bottom surface of the TI structures in the first group at maximum indenter displacement.

otherwise lead to premature material failure. Therefore, the structure can undergo larger deformation and absorb more energy prior to failure. Similar stress delocalisation is observed in other TI plates, with the extent influenced by the base polygon shape. The TI plate with a hexagonal base polygon shape exhibits higher concentration of stress around the central elements compared to other TI plates, with notable stress concentrations at their interfaces. This phenomenon can be explained by the crucial role of a TI element's contact area in load transfer and stress distribution within TI assemblies. A larger contact area enhances stress delocalisation by distributing loads more evenly across the structure, reducing stress concentrations and the likelihood of premature failure. The element with a triangular base polygon shape has the highest contact area (6584 mm^2) and contact area ratio (1.32) (Table 1), facilitating balanced load transfer and uniform stress distribution. This reduces stress accumulation and enhances energy

absorption. In contrast, despite having more interfaces, the TI element with a hexagonal base polygon shape has smallest contact area (4700 mm^2) and the lowest contact area ratio (0.92), leading to stress confinement within a smaller region. This increases the likelihood of stress intensification at critical points, making the structure more susceptible to failure in certain elements. The reduced contact area may also limit the ability to redistribute load efficiently, further compromising structural integrity under impact loading conditions. These results underscore the critical role of base polygon shape and contact area in optimising the energy absorption and stress distribution performance of TI assemblies.

In the first group, the size factor (volume) and interface morphology (curvature) remain consistent, allowing the contact area and contact area ratio to serve as the key metrics for assessing the interlocking effect. To further evaluate the effects of these two metrics, Fig. 13 illustrates the
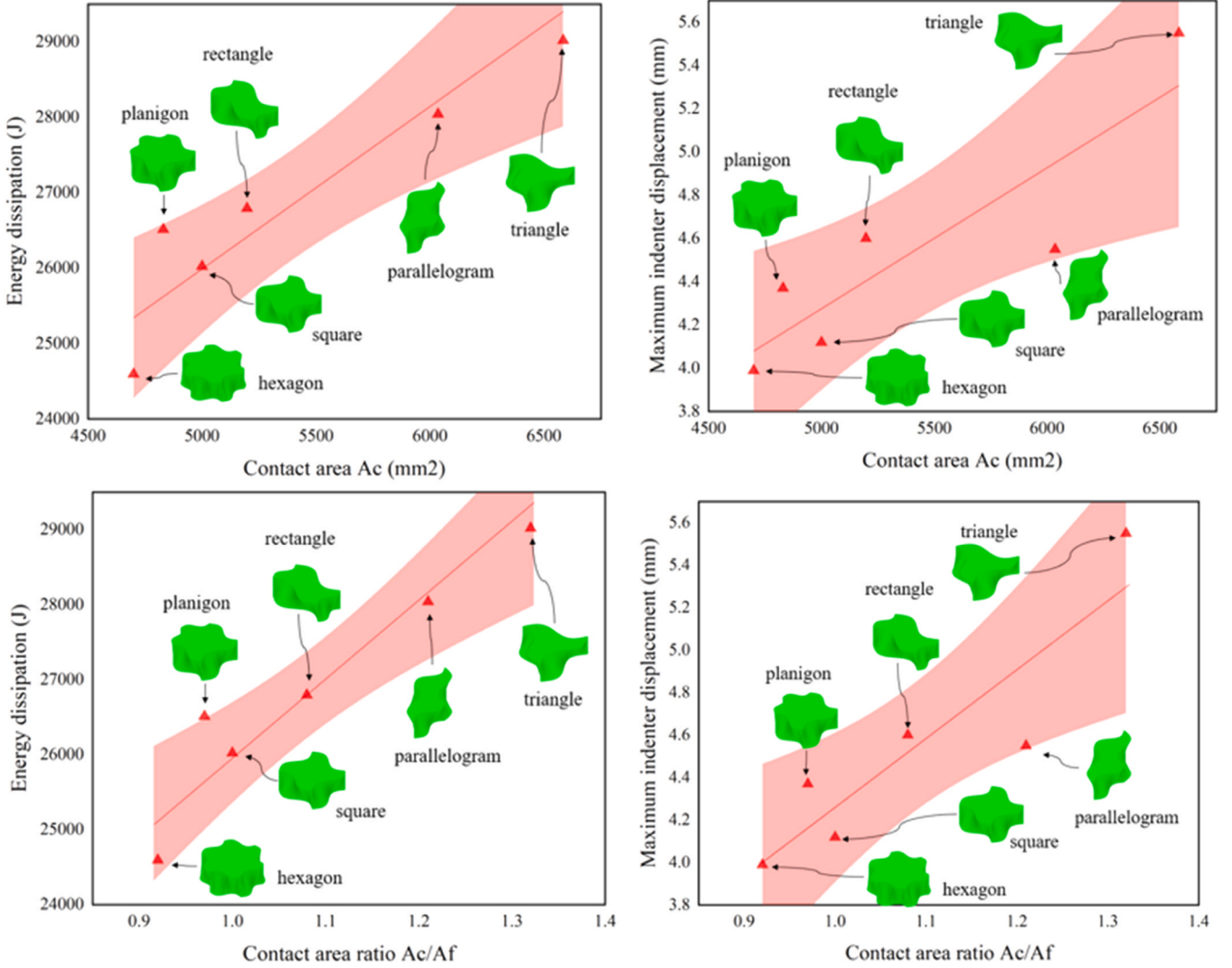
Fig. 13. Relationship of mechanical performance with contact area and contact area ratio in the first group.

relationship between mechanical performance (energy dissipation and maximum indenter displacement) and both the contact area A_c and the contact area ratio A_c/A_f (values provided in Table 1). As can be seen, both energy dissipation and maximum indenter displacement increase almost linearly with the contact area A_c. As the contact area increases, the ability of the structure to absorb impact energy improves, leading to higher energy dissipation and increased displacement. This behaviour can be attributed to the enhanced interlocking effect, where a larger contact area allows more effective engagement between individual elements, facilitating better force distribution and energy transfer across the structure. For example, the structure with a triangular base polygon shape exhibits the greatest deformation capacity and highest energy dissipation due to its larger inter-element contact area, which enhances material jamming and frictional engagement, thereby strengthening the interlocking effect. The simulation results show a strong correlation, as evidenced by the majority of data points falling within the 95 % confidence band (red area in Fig. 13), reinforcing the reliability of the contact area as an indicator of understanding the mechanical performance of TI structures under impact loading. The contact area ratio A_c/A_f shows an even stronger linear correlation with energy dissipation and maximum indenter displacement than the contact area. This is because the ratio highlights the contribution of curved interfaces relative to the total surface area. By normalising the curved contact area against the flat area, the ratio more accurately captures the efficiency of the

interlocking geometry in enhancing energy dissipation and stress redistribution. As a result, it serves as a more representative and reliable metric for assessing interlocking efficiency. Overall, both A_c and A_c/A_f effectively capture the interplay between geometric attributes and mechanical performance, making them valuable indicators for optimising TI structure designs.

4.1.2. Failure mode

Fig. 14 illustrates the deformation patterns of the TI assemblies in the first groups under impact loading from 1 m drop height. All TI assemblies maintain structural integrity during deflection, with the central element remaining secured until material failure. This behaviour is significantly different from that of the polyhedral assemblies [46,47], which often experience central element pullout. The geometric interlocking created by the curved interfaces enhances the cohesion between elements, improving overall structural integrity.

To understand failure mechanism and damage evolution, structural responses under impact from a 3 m drop height are analysed. This height results in more pronounced material failure, allowing for clear observation of characteristic failure modes. Fig. 15 shows the damage distributions on the bottom surfaces of the TI assemblies. For the TI plate with a triangular base polygon shape, damage is widely distributed along the element interfaces across the assembly. This can be attributed to the larger contact area of the triangular configuration, which
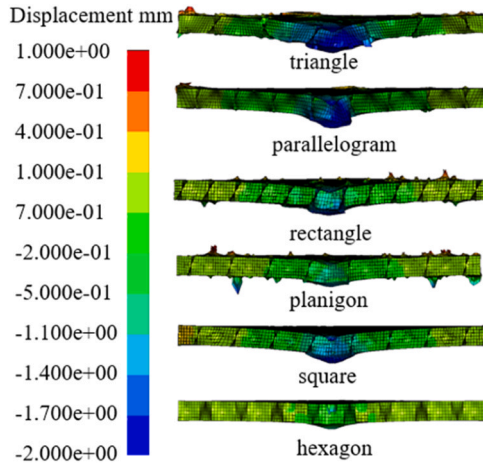
Fig. 14. Deformation of TI structures in the first group under impact from 1 m drop height.
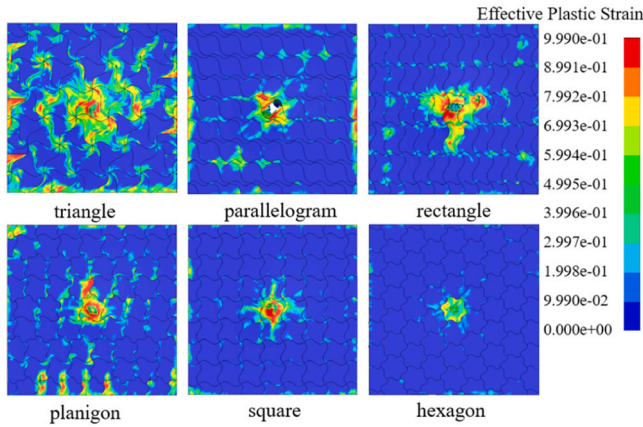

Fig. 15. Damage patterns on the bottom surfaces of TI structures in the first group under 3 m indenter impact.

facilitates more effective stress transfer between adjacent elements. However, the sharp edges of triangular elements create stress concentrations, serving as preferential sites for crack initiation. Once initiated, cracks propagate along the curved interfaces, where relative sliding and opening between adjacent elements induce further interface debonding and facilitate crack growth. In contrast, the structure with a hexagonal base polygon shape exhibits a different failure pattern. Due to its smaller contact area, the hexagonal configuration has reduced capability to redistribute impact-induced stresses to neighbouring elements. Consequently, damage is primarily confined to the element under direct impact, and cracks propagate within individual elements rather than across interfaces. This results in shorter crack paths and a more contained damage zone, reflecting a less interconnected failure mechanism with minimal inter-element debonding. The damage characteristics of the other designs (rectangular, square, and parallelogram) exhibit intermediate behaviour, balancing between localised element failure and interface-driven damage evolution.

4.2. TI elements with different interface morphologies

4.2.1. Mechanical performance and interlocking metrics

This section investigates the mechanical responses of TI structures with different interface morphologies (the second group) under impact loading. Fig. 16 shows the energy dissipation, maximum indenter displacement, and impact force-displacement behaviour of TI plates subjected to impact from a 1 m drop height. The energy dissipation of the TI structures, ranked from highest to lowest, is as follows: twice-amplitude, layered, hierarchical, Bezier, half-wave, and full-wave [Fig. 16(a)]. The maximum indenter displacement follows the same order as energy dissipation [Fig. 16(a)], indicating that structures with higher energy dissipation also have greater deformation capacity. Fig. 16(b) shows that the force-displacement curves are similar across all designs in the second group. This is attributed to the use of the same base polygon shape, which governs deformation mode and load paths. As a result, plates with identical base polygon shape exhibit comparable force-displacement behaviour under the same loading conditions.

Fig. 17 presents the stress distributions on the bottom surfaces of the second group of TI structures, showing variations across designs with six different interface morphologies. TI structures featuring interfaces with higher critical inclination angle factors, such as the twice-amplitude (1.12) and layered (1.03) designs, exhibit broader stress propagation,
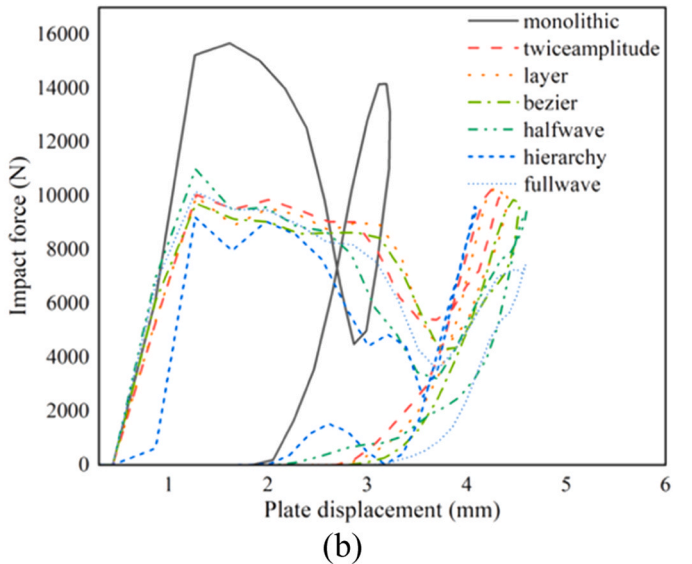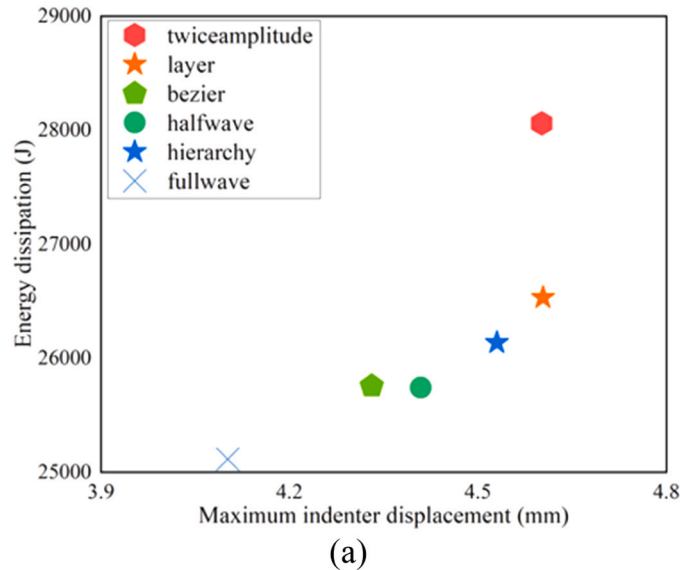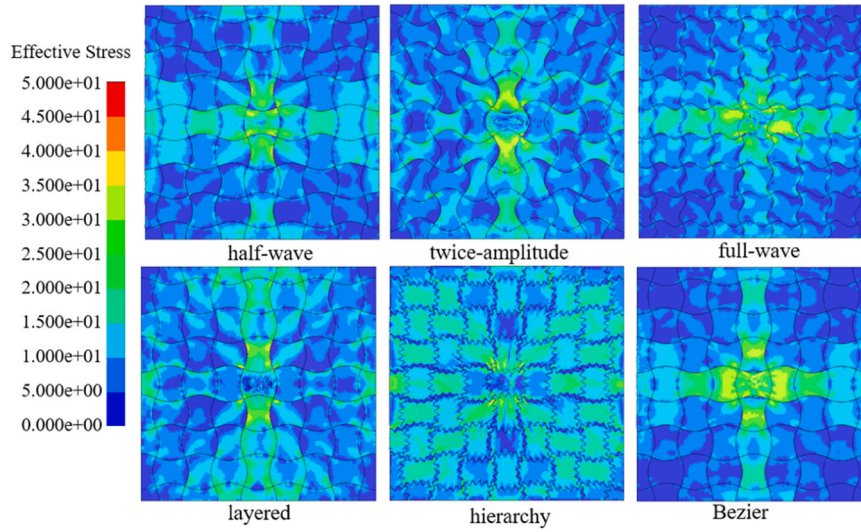

Fig. 16. Energy dissipation-maximum indenter displacement relationships and impact force-displacement curves of the second group of TI structures at a drop height of 1.0 m.

Fig. 17. Stress distribution on the bottom surface of the TI structures in the second group at maximum displacement.

attributed to stronger interlocking that facilitates load dispersion across a wider region. In contrast, lower critical inclination angle factors, as seen in the full-wave (0.25) and Bezier (0.56) interfaces, result in stress concentrations and the formation of dominant load paths. The hierarchical interface (0.64), characterised by its self-similar sawtooth geometry, overcomes this limitation by promoting multiscale stress reflection and redistribution, thereby enhancing stress uniformity. These results indicate that higher critical inclination angle factors promote effective stress transfer, while morphologies incorporating hierarchical features contribute to more uniform stress fields through geometrically induced stress diffusion mechanisms.

Although contact area and contact area ratio are effective metrics for evaluating TI elements with different base polygon shapes, they cannot distinguish between elements in the second group, where the base polygon shape remains the same. In this group, the critical inclination angle factor is used to evaluate mechanical performance, while Gaussian curvature is employed to assess interface failure (discussed in Section 4.2.2). These two metrics can detect differences in surface curvature and alignment, providing a more accurate examination of interface mechanical performance. Fig. 18 illustrates the relationships between energy dissipation, maximum indenter displacement, and the critical inclination angle factor. As can be seen, both energy dissipation and maximum indenter displacement exhibit a strong linear correlation with the critical inclination angle factor. A higher value of critical inclination angle factor enhances interlocking and load transfer efficiency between adjacent elements, leading to improved deformation capacity and energy dissipation of TI plates. This effect is achieved through increased interface friction and material jamming, which contribute to greater stress redistribution. The improved deformation capacity allows the structure to absorb more energy. The observed linear trends indicate that the critical inclination angle factor can serve as a key design parameter for optimising the mechanical performance of TI structures with the same base polygon shape.

4.2.2. Failure mode

Fig. 19 illustrates the damage patterns on the bottom surfaces and the corresponding interfacial stress distributions of the second group of TI structures subjected to impact loading from a 3 m drop height. All six TI structures exhibit localised failure modes [Fig. 19(a)], with the extent and location of damage zones governed by the specific interface generation method. The spatial distribution of Gaussian curvature along the interfaces plays a critical role in damage localisation, as evidenced by
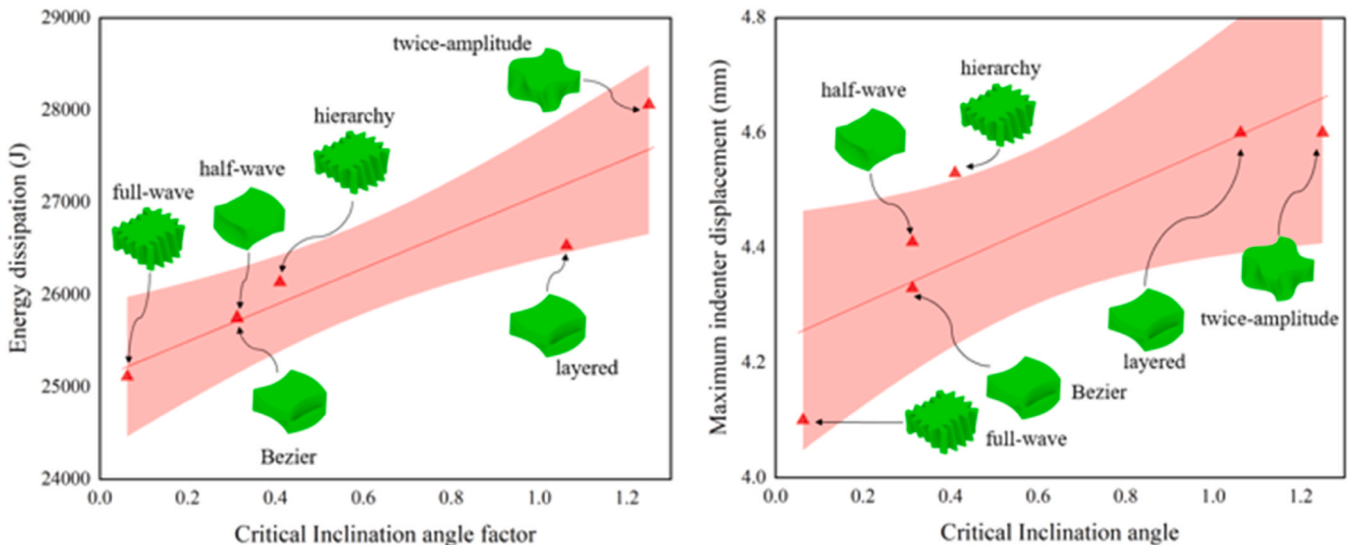

Fig. 18. Relationship of mechanical performance with critical inclination angle factor in the second group.
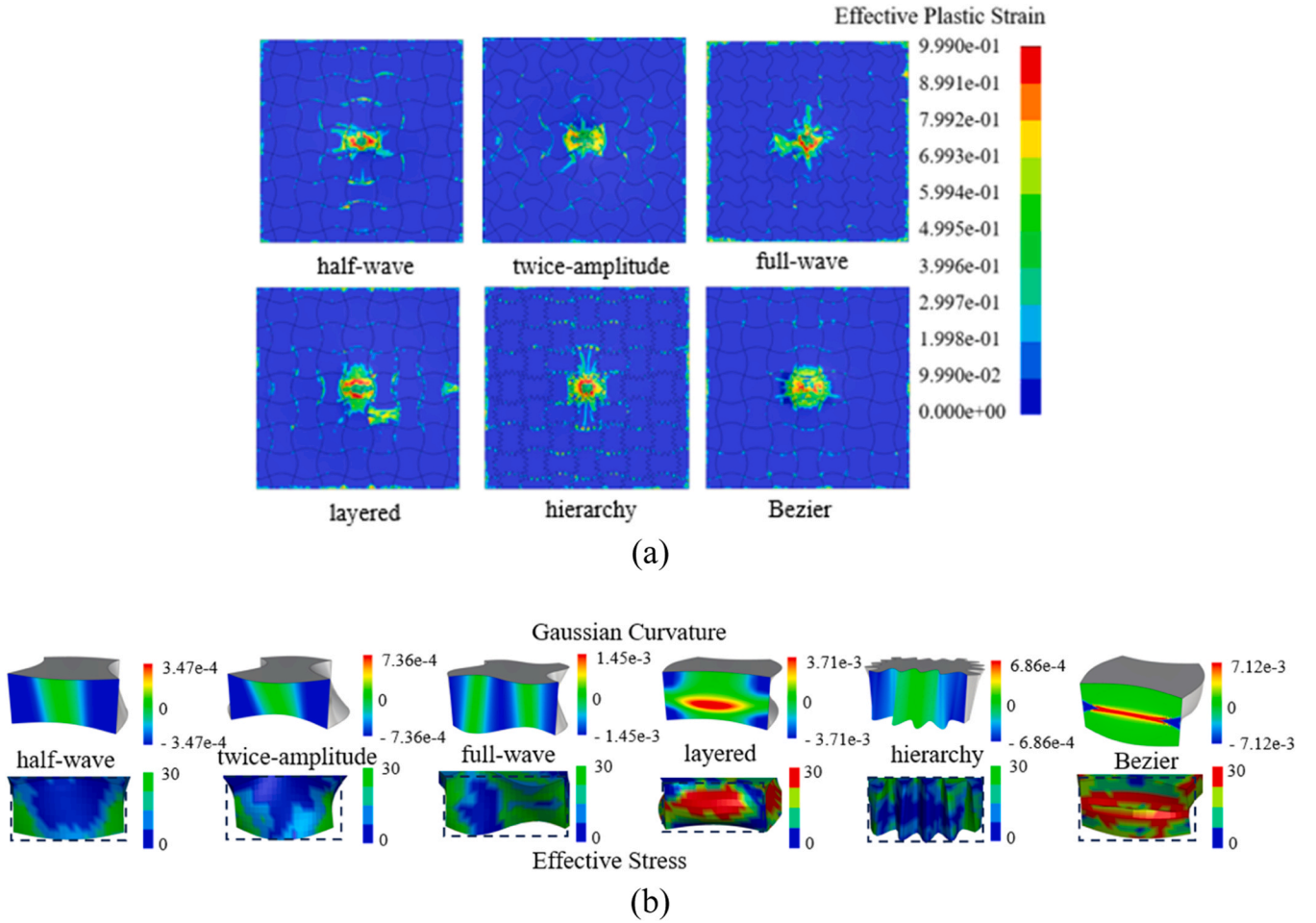
Fig. 19. Failure of TI structures and elements in the second group: (a) damage patterns on the bottom surface, and (b) Gaussian curvature and effective stress distributions on interfaces.

the strong correlation between high-curvature regions and stress concentrations observed in Fig. 19(b). These curvature-induced geometric features act as stress intensifiers, serving as preferential sites for crack initiation. Following initiation, crack propagation is influenced by the morphology of the interlocking interfaces. Cracks tend to propagate along inter-element interfaces and through sharp angles, where relative sliding, tensile opening, or mixed-mode separation is more likely to occur. These results suggest that Gaussian curvature serves as a predictive morphological parameter, linking interface geometry with stress distribution and damage evolution. By mapping curvature distributions, regions susceptible to high stress can be pre-identified, enabling more informed and performance-oriented interface design. Overall, these findings underscore the dominant influence of interface morphology on failure mechanisms and highlight Gaussian curvature as a key metric for failure prediction and design optimisation for TI structures.

5. Conclusions

This study systematically investigates the impact performance of plate-like TI structures composed of curved-interface elements, with a particular focus on the influence of base polygon shape and interface morphology. Two groups of TI configurations are examined to elucidate the role of geometric parameters in governing mechanical behaviour under impact loading. To quantitatively assess interlocking efficacy, four interlocking metrics are proposed, including contact area A_c, contact area ratio A_c/A_f, Gaussian curvature K, and critical inclination angle factor. These metrics provide direct insights into the relationship be-

tween interface geometry and mechanical performance, and have proven effective in guiding the rational design and optimisation of TI structures. The key findings are summarised as follows:

1. The base polygon shape has a pronounced impact on the mechanical behaviour of TI structures by affecting the element contact area and load transfer efficiency. The structure with triangular base polygon offers larger contact area, promoting more uniform stress distribution and enhanced energy absorption. The structure with hexagonal base polygon shape tends to exhibit localised stress and damage.

2. Interface morphology plays a critical role in the mechanical performance of TI structures by controlling load dispersion. Designs with larger critical inclination angle factors facilitate broader stress propagation and improve energy dissipation.

3. The energy dissipation capacity and maximum deflection of TI structures exhibit a strong linear correlation with both the contact area (or contact area ratio) and the critical inclination angle factor. Increase in either parameter promotes more extensive deformation and, consequently, improved energy absorption capacity of the structure.

4. Gaussian curvature provides valuable insight into the interfacial stress distribution, with regions of high curvature consistently associated with stress concentrations. This correlation enables the prediction of localised failure zones and supports the development of targeted reinforcement strategies to enhance structural performance.

While the proposed interlocking metrics are derived from sinusoidal interface profiles, they capture fundamental geometric attributes governing confinement and load transfer. Future studies will explore their applicability to non-sinusoidal and more complex interface geometries.

Additionally, a systematic investigation into the effects of varying friction coefficients on interfacial behaviour and their influence on the correlation between interlocking metrics and structural performance will be conducted. The implementation of multi-layer configurations will also be examined to evaluate the impact of interlayer interactions on force transfer pathways, confinement, and energy dissipation mechanisms. Finally, future research will extend this framework to other material systems, such as ceramics and metals, by employing appropriate constitutive material models to capture their distinct mechanical responses and failure mechanisms. This includes addressing material-specific behaviours like brittle fracture in ceramics and plastic deformation or yielding in ductile metals.

CRediT authorship contribution statement

Siya Wang: Writing – review & editing, Writing – original draft, Validation, Methodology, Investigation, Formal analysis, Data curation, Conceptualization. **Xiaoshan Lin:** Writing – review & editing, Validation, Supervision, Resources, Project administration, Methodology, Investigation, Funding acquisition, Conceptualization. **Yi Min Xie:** Writing – review & editing, Supervision, Methodology, Conceptualization. **Y.X. Zhang:** Writing – review & editing, Supervision, Methodology.

Declaration of Competing Interest

The authors declare that they have no known competing financial interests or personal relationships that could have appeared to influence the work reported in this paper.

Acknowledgement

Appendix

Fig. A.1 illustrates the formulas for calculating the contact area and contact area ratio of the elements in the first TI element group. a_x represents the edge length of different base polygon shapes, and A refers to the area of the polygonal surface. The curve function applied to the polygon edges is symmetrical, which ensures that the area of the protrusions equals the area of the recesses, thereby maintaining the modified prototile's area equivalent to that of the original base polygon.
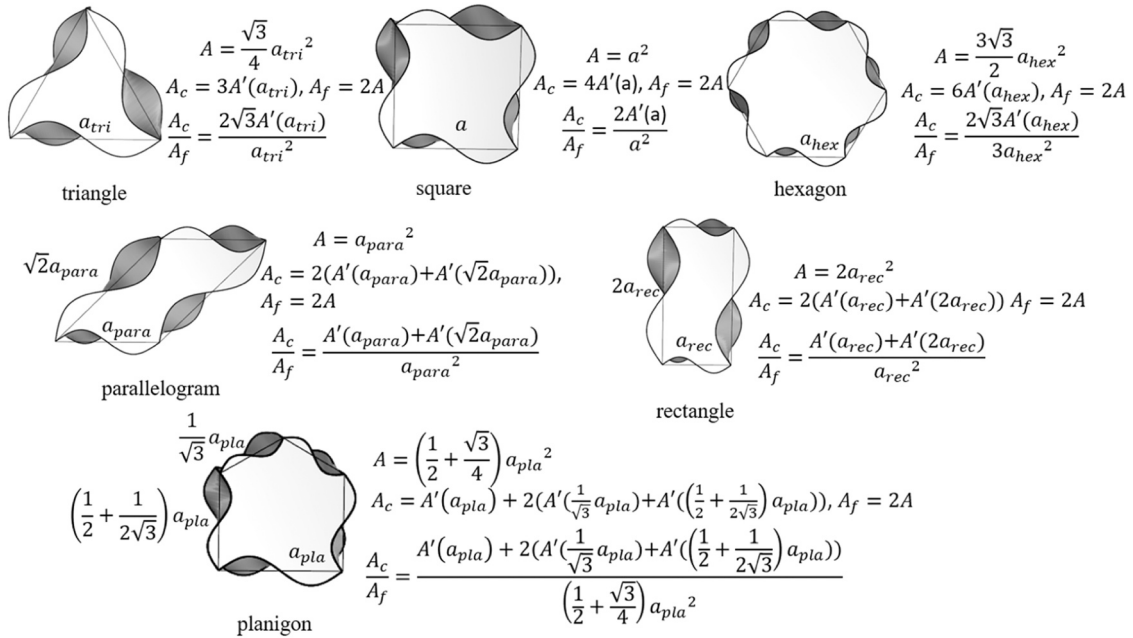

triangle
$$A = \frac{\sqrt{3}}{4} a_{tri}^2$$
$$A_c = 3A'(a_{tri}), A_f = 2A$$
$$\frac{A_c}{A_f} = \frac{2\sqrt{3}A'(a_{tri})}{a_{tri}^2}$$

square
$$A = a^2$$
$$A_c = 4A'(a), A_f = 2A$$
$$\frac{A_c}{A_f} = \frac{2A'(a)}{a^2}$$

hexagon
$$A = \frac{3\sqrt{3}}{2} a_{hex}^2$$
$$A_c = 6A'(a_{hex}), A_f = 2A$$
$$\frac{A_c}{A_f} = \frac{2\sqrt{3}A'(a_{hex})}{3a_{hex}^2}$$

parallelogram
$$A = a_{para}^2$$
$$A_c = 2(A'(a_{para})+A'(\sqrt{2}a_{para})), \quad A_f = 2A$$
$$\frac{A_c}{A_f} = \frac{A'(a_{para})+A'(\sqrt{2}a_{para})}{a_{para}^2}$$

rectangle
$$A = 2a_{rec}^2$$
$$A_c = 2(A'(a_{rec})+A'(2a_{rec})) \quad A_f = 2A$$
$$\frac{A_c}{A_f} = \frac{A'(a_{rec})+A'(2a_{rec})}{a_{rec}^2}$$

planigon
$$A = \left(\frac{1}{2}+\frac{\sqrt{3}}{4}\right) a_{pla}^2$$
$$A_c = A'(a_{pla}) + 2\left(A'(\frac{1}{\sqrt{3}}a_{pla})+A'(\left(\frac{1}{2}+\frac{1}{2\sqrt{3}}\right)a_{pla})\right), A_f = 2A$$
$$\frac{A_c}{A_f} = \frac{A'(a_{pla}) + 2\left(A'(\frac{1}{\sqrt{3}}a_{pla})+A'(\left(\frac{1}{2}+\frac{1}{2\sqrt{3}}\right)a_{pla})\right)}{\left(\frac{1}{2}+\frac{\sqrt{3}}{4}\right)a_{pla}^2}$$

Fig. A.1. Contact area and contact area ratio of TI elements in the first group

The curve function for the square prototile is defined by Eq. (A.1). The curve functions for the top and bottom edges of the other elements are given in Eqs. (A.2) and (A.3), respectively. The volume, height, and interface morphology of the elements are kept constant.

$$\text{Square prototile}: f(x) = 6\sin\frac{2\pi x}{a}, \; x \in [0, a] \tag{A.1}$$

To create the concavo-convex interface morphology, the curve function of the top and bottom edges must be in opposite directions [29], yielding:

$$\text{Top edge of the other elements}: \quad f_{top}(x) = 6\frac{a_x}{a}\sin\frac{2\pi x}{a_x}, \quad z = \frac{a}{2}, x \in [0, a_x] \tag{A.2}$$

$$\text{Bottom edge of the other elements}: \quad f_{bottom}(x) = -6\frac{a_x}{a}\sin\frac{2\pi x}{a_x}, \quad z = 0, x \in [0, a_x] \tag{A.3}$$

where a is the edge length of the square prototile, a_x refers to the edge length of the corresponding TI elements, and (x, y, z) represents the three-dimensional coordinates, as shown in Fig. 1(b).

The surface generated by lofting between the top and bottom edges can be parameterised as follows:

$$r(x,v) = \left(x, v \bullet 6 \frac{a_x}{a} \sin\left(\frac{2\pi x}{a_x}\right), v \bullet \frac{a}{2} \right) \tag{A.4}$$

where $v \in [0,1]$ is the parameter that interpolates between the top and bottom edges.

Therefore, the area of a single curved interface $A'(a_x)$ can be calculated using the following equation:

$$A'(a_x) = \int_0^1 \int_0^{a_x} \left\| \frac{\partial r}{\partial x} \times \frac{\partial r}{\partial v} \right\| \mathrm{d}x\mathrm{d}v = \int_0^1 \int_0^{a_x} \sqrt{ \left(\frac{a}{2} \bullet 6 \frac{2\pi}{a} \cos\left(\frac{2\pi x}{a_x}\right) \right)^2 + \left(\frac{a}{2}\right)^2 + \left(6 \frac{a_x}{a} \sin\left(\frac{2\pi x}{a_x}\right) \right)^2 } \mathrm{d}x\mathrm{d}v \tag{A.5}$$

By using the substitution $u = \frac{2\pi x}{a_x}$, where $\mathrm{d}u = \frac{2\pi}{a_x}\mathrm{d}x$, and solving the integral, the area is proportional to a_x^2, yielding:

$$A'(a_x) = \frac{a_x{}^2}{2\pi} \int_0^1 \int_0^{a_x} \sqrt{ \left(\frac{9\pi^2}{a_x{}^2}\cos^2(u) \right) + \left(\frac{a}{2a_x}\right)^2 + \frac{36\sin^2(u)}{a^2} } \mathrm{d}u\mathrm{d}v \tag{A.6}$$

Thus, a simplified relationship between the contact area and the edge length is established:

$$A'(a_x) = C \bullet a_x{}^2 \tag{A.7}$$

where C is given as:

$$C = \frac{1}{2\pi} \int_0^1 \int_0^{a_x} \sqrt{ \left(\frac{9\pi^2}{a_x{}^2}\cos^2(u) \right) + \left(\frac{a}{2a_x}\right)^2 + \frac{36\sin^2(u)}{a^2} } \mathrm{d}u\mathrm{d}v \tag{A.8}$$

Thus, for elements with different base polygonal patterns, the ratio A_c/A_f can be expressed in terms of C as follows:

Triangle : $\dfrac{A_c}{A_f} = 2\sqrt{3}C = 3.4C$

Square : $\dfrac{A_c}{A_f} = 2C$

Hexagon : $\dfrac{A_c}{A_f} = \dfrac{2\sqrt{3}}{3}C = 1.2C$

Parallelogram : $\dfrac{A_c}{A_f} = 3C$

Planigon : $\dfrac{A_c}{A_f} = \dfrac{28 + 4\sqrt{3}}{6 + 3\sqrt{3}}C = 3.12C$

Rectangle : $\dfrac{A_c}{A_f} = 2.5C$

Data Availability

Data will be made available on request.

References

[1] Barthelat F. Architectured materials in engineering and biology: fabrication, structure, mechanics and performance. Int Mater Rev 2015;60(8):413–30. https://doi.org/10.1179/1743280415Y.0000000008.

[2] Estrin Y, Dyskin AV, Pasternak E. Topological interlocking as a material design concept. Mater Sci Eng C 2011;31(6):1189–94. https://doi.org/10.1016/j.msec.2010.11.011.

[3] Dyskin AV, Estrin Y, Kanel-Belov AJ, Pasternak E. A new concept in design of materials and structures: assemblies of interlocked tetrahedron-shaped elements. Scr Mater 2001;44(12):2689–94. https://doi.org/10.1016/S1359-6462(01)00968-X.

[4] Dyskin AV, Estrin Y, Pasternak E, Khor HC, Kanel-Belov AJ. The principle of topological interlocking in extraterrestrial construction. Acta Astronaut 2005;57 (1):10–21. https://doi.org/10.1016/j.actaastro.2004.12.005.

[5] Dyskin AV, Pasternak E, Estrin Y. Mortarless structures based on topological interlocking. Front Struct Civ Eng 2012. https://doi.org/10.1007/s11709-012-0156-8.

[6] Dyskin AV, Estrin Y, Pasternak E. Topological interlocking materials. in Springer Series in Materials Science, vol. 282. In: Estrin Y, Bréchet Y, Dunlop J, Fratzl P, editors. Architectured Materials in Nature and Engineering, 282. Cham: Springer International Publishing; 2019. p. 23–49. https://doi.org/10.1007/978-3-030-11942-3_2. in Springer Series in Materials Science, vol. 282.

[7] Krishnamurthy V, et al. LayerLock: Layer-Wise Collision-Free Multi-Robot additive manufacturing using topologically interlocked Space-Filling shapes. Comput Aided Des 2022;152:103392. https://doi.org/10.1016/j.cad.2022.103392.

[8] Piirainen VY, Estrin Y. New approach to road construction in Oil-Producing regions of Western siberia. Iop Conf Ser Earth Environ Sci 2017;87:072003. https://doi.org/10.1088/1755-1315/87/7/072003.

[9] Schapira Y, Chernin L, Shufrin I. Blast energy absorption in topological interlocking elastic columns. Mech Adv Mater Struct 2022:1–13. https://doi.org/10.1080/15376494.2022.2127038.

[10] Ali M, Briet R, Chouw N. Dynamic response of mortar-free interlocking structures. Constr Build Mater 2013;42:168–89. https://doi.org/10.1016/j.conbuildmat.2013.01.010.

[11] Mahoney K, Siegmund T. Mechanics of tubes composed of interlocking building blocks. 103654–103654 Int J Eng Sci 2022;174. https://doi.org/10.1016/j.ijengsci.2022.103654.

[12] Siegmund T, Barthelat F, Cipra R, Habtour E, Riddick J. Manufacture and mechanics of topologically interlocked material assemblies. Appl Mech Rev 2016; 68(4):040803. https://doi.org/10.1115/1.4033967.

[13] В. Ю. Пиирайнен and Ю. З. Эстрин, "Topological interlocking as a principle of engineering design in consruction of marine and coastal structures," DOAJ (DOAJ: Directory of Open Access Journals), 2017, doi: https://doi.org/10.25515/pmi.2017.4.480.

[14] Tavoosi Gazkoh M, Lin X, Zhou A. Advancing topological interlocking structures: recent developments, applications, and challenges in civil engineering. Int J Concr Struct Mater 2024;18(1):91. https://doi.org/10.1186/s40069-024-00735-3.

[15] Rezaee Javan A, Seifi H, Lin X, Xie YM. Mechanical behaviour of composite structures made of topologically interlocking concrete bricks with soft interfaces. Mater Des 2020;186:108347. https://doi.org/10.1016/j.matdes.2019.108347.

[16] Xu W, Lin X, Li P, Wu Y-F, Xie YM. Impact behaviour of tunnel lining assembled from non-planar interlocking steel fibre reinforced concrete bricks. Eng Struct 2023;296:116907. https://doi.org/10.1016/j.engstruct.2023.116907.

[17] Han W, Zhang C, Sun J, Zhou C, Ding L. Experimental and numerical study on the structural behavior of assembled interlocking lunar landing pad. Acta Astronaut 2023;207:77–88. https://doi.org/10.1016/j.actaastro.2023.03.001.

[18] Estrin Y, Krishnamurthy VR, Akleman E. Design of architectured materials based on topological and geometrical interlocking. J Mater Res Technol 2021;15: 1165–78. https://doi.org/10.1016/j.jmrt.2021.08.064.

[19] Molotnikov A, Estrin Y, Dyskin AV, Pasternak E, Kanel-Belov AJ. Percolation mechanism of failure of a planar assembly of interlocked osteomorphic elements. Eng Fract Mech 2007;74(8):1222–32. https://doi.org/10.1016/j.engfracmech.2006.07.012.

[20] Djumas L, Molotnikov A, Simon GP, Estrin Y. Enhanced mechanical performance of Bio-Inspired hybrid structures utilising topological interlocking geometry. Sci Rep 2016;6(1):26706. https://doi.org/10.1038/srep26706.

[21] A.V. Dyskin, Y. Estrin, A.J. Kanel-Belov, and E. Pasternak, 'Toughening by Fragmentation—How Topology Helps', Adv. Eng. Mater., vol. 3, no. 11, p. 885,2001, doi: 10.1002/1527-2648(200111)3:11<885::AID-ADEM885>3.0.CO;2-P.

[22] Molotnikov A, Gerbrand R, Bouaziz O, Estrin Y. Sandwich panels with a core segmented into topologically interlocked elements. Adv Eng Mater 2013;15(8): 728–31. https://doi.org/10.1002/adem.201300002.

[23] Djumas L, Simon GP, Estrin Y, Molotnikov A. Deformation mechanics of non-planar topologically interlocked assemblies with structural hierarchy and varying geometry. Sci Rep 2017;7(1):11844. https://doi.org/10.1038/s41598-017-12147-3.

[24] Rezaee Javan A, Seifi H, Xu S, Ruan D, Xie YM. The impact behaviour of plate-like assemblies made of new interlocking bricks: an experimental study. Mater Des 2017;134:361–73. https://doi.org/10.1016/j.matdes.2017.08.056.

[25] Xu W, Wu H, Lin X, Min Xie Y. Numerical simulation and comparative design of non-planar interlocking fibre reinforced concrete bricks for tunnel lining structure under impact loading. Tunn Undergr Space Technol 2025;155:106184. https://doi.org/10.1016/j.tust.2024.106184.

[26] Koureas I, Pundir M, Feldfogel S, Kammer DS. Beam-like topologically interlocked structures with hierarchical interlocking. J Appl Mech 2023;90(8):081008. https://doi.org/10.1115/1.4062348.

[27] Dalaq AS, Barthelat F. Manipulating the geometry of architectured beams for maximum toughness and strength. Mater Des 2020;194:108889. https://doi.org/10.1016/j.matdes.2020.108889.

[28] Koureas I, Pundir M, Feldfogel S, Kammer DS. The key to the enhanced performance of slab-like topologically interlocked structures with non-planar blocks. Int J Solids Struct 2023;285:112523. https://doi.org/10.1016/j.ijsolstr.2023.112523.

[29] Wang S, Lin X, Zhang YX, Xie YM. A generalised framework for designing topological interlocking structures from monomorphic elements. Eng. Struct. 2025; 338:120607. https://doi.org/10.1016/j.engstruct.2025.120607.

[30] Ma X, Zhang DZ, Wei D, Li Z, Ban Z. Investigation of surface curvature distribution characteristic on the mechanical properties of 3D printed lattice structures. Int J Adv Manuf Technol 2023;128(3–4):1577–96. https://doi.org/10.1007/s00170-023-11630-8.

[31] Yang N, Wei H, Mao Z. Tuning surface curvatures and young's moduli of TPMS-based lattices independent of volume fraction. Mater Des 2022;216:110542. https://doi.org/10.1016/j.matdes.2022.110542.

[32] Hegarty-Cremer SGD, Simpson MJ, Andersen TL, Buenzli PR. Modelling cell guidance and curvature control in evolving biological tissues. J Theor Biol 2021; 520:110658. https://doi.org/10.1016/j.jtbi.2021.110658.

[33] Mirkhalaf M, Zhou T, Barthelat F. Simultaneous improvements of strength and toughness in topologically interlocked ceramics. Proc Natl Acad Sci 2018;115(37): 9128–33. https://doi.org/10.1073/pnas.1807272115.

[34] Ministry of Housing and Urban-Rural Development of China (MOHURD). Code for seismic design of buildings (GB 50011-2010). Beijing: China Architecture & Building Press; 2010.

[35] American Society of Civil Engineers (ASCE). Minimum design loads and associated criteria for buildings and other structures (ASCE/SEI 7-16)'. Reston, VA: ASCE; 2017.

[36] Huang Y, Jiang J. A critical review of von mises criterion for compatible deformation of polycrystalline materials. Crystals 2023;13(2):244. https://doi.org/10.3390/cryst13020244.

[37] European Committee for Standardization (CEN). Eurocode 3: design of steel structures – part 1-1: general rules and rules for buildings (EN 1993-1-1)'. Brussels: CEN; 2005.

[38] Petrosian LG. Dynamics of structures: oscillations/vibrations. Cham: Springer Nature Switzerland; 2024. https://doi.org/10.1007/978-3-031-63539-7.

[39] Rezaee Javan A, Seifi H, Xu S, Lin X, Xie YM. Impact behaviour of plate-like assemblies made of new and existing interlocking bricks: a comparative study. Int J Impact Eng 2018;116:79–93. https://doi.org/10.1016/j.ijimpeng.2018.02.008.

[40] Y. Wu, J.E. Crawford, and J.M. Magallanes, 'Performance of LS-DYNA® concrete constitutive models'.

[41] Murray YD, Abu-Odeh AY, Bligh RP. Evaluation of LS-DYNA concrete material model 159 (No. FHWA-HRT-05-063). United States. Federal highway administration. Office of Research, Development, and Technology; 2007.

[42] MANUAL, K.U.S. (2021). LS-DYNA keyword User's manual volume II: material models. LSTC Co., Livermore, CA.

[43] Lin X, Zhang YX. Nonlinear finite element analysis of FRP-strengthened reinforced concrete panels under blast loads. Int J Comput Methods 2016;13(04):1641002. https://doi.org/10.1142/S0219876216410024.

[44] Xu W, Lin X, Xie YM. A novel non-planar interlocking element for tubular structures. Tunn Undergr Space Technol 2020;103:103503. https://doi.org/10.1016/j.tust.2020.103503.

[45] Kannikachalam NP, Marin Peralta PS, Snoeck D, De Belie N, Ferrara L. Assessment of impact resistance recovery in ultra high-performance concrete through stimulated autogenous self-healing in various healing environments. Cem Concr Compos 2023;143:105239. https://doi.org/10.1016/j.cemconcomp.2023.105239.

[46] Mirkhalaf M, Sunesara A, Ashrafi B, Barthelat F. Toughness by segmentation: fabrication, testing and micromechanics of architectured ceramic panels for impact applications. Int J Solids Struct 2019;158:52–65. https://doi.org/10.1016/j.ijsolstr.2018.08.025.

[47] Dalaq AS, Barthelat F. Strength and stability in architectured spine-like segmented structures. Int J Solids Struct 2019;171:146–57. https://doi.org/10.1016/j.ijsolstr.2019.04.012.